13th ewtec 2019 Proceedings of the 13th European Wave and Tidal Energy Conference 1-6 Sept 2019, Naples, Italy

Variable-fidelity CFD modelling of horizontal-axis tidal turbines and arrays

Giulio Dubbioso, Francesco Salvatore, Zohreh Sarichloo, Danilo Calcagni, Roberto Muscari, Ralf Starzmann

***Abstract*—The assessment of a design-oriented hydrodynamics model for horizontal axis tidal turbines is addressed. The methodology is based on a Boundary Integral Equation Model with a simple viscous flow correction (BIEM-VFC) and is valid to analyse the three-dimensional flow around a turbine in arbitrary onset flow at computational costs comparable to standard blade element methods. A validation study is performed by using benchmark data from full viscous flow simulations by RANS. Numerical results by BIEM-VFC are compared with RANS predictions of turbine global performance, thrust and power, as well as local flow quantities describing pressure distributions and wall streamlines on blades and trailing vorticity path in the wakefield. The validation study demonstrates that BIEM-VFC predictions of both global and local flow quantities are comparable with those obtained from more complex full viscous flow simulations for a range of turbine operating conditions where viscosity effects are significant but blades are free from massive separation and stall. For operating conditions characterized by blade stall, BIEM-VFC fails to describe local flow details while qualitative approximations of global loads are given.**

***Index Terms*—Tidal energy, horizontal-axis turbines, hydrodynamics, computational models, RANS, Boundary Integral Equation Model, CFD validation**

I. Introduction

TIDAL turbines operate in flows characterized by strong turbulence, shear and vortical structures covering a large range of scales [1]. This affects hydrodynamic performance and structural integrity, as well as the dynamics of rotor wakes in arrays [2]. Computational Fluid Dynamics (CFD) models based on the numerical solution of the Navier-Stokes equations provide the most general approach to describe turbine hydrodynamics in viscous, turbulent flows. Recent literature (see, *e.g.*, [3], [4]) demonstrates that CFD simulations can be used as virtual flume tank experiments in which both turbine global performance as well as details of the interaction between turbine and the surrounding flow are obtained. This is achieved at computational costs that are unaffordable for design applications when a complex configuration has to be studied, as in the case of turbine arrays or clusters [5].

A classical approach to mitigate the computational burden is to decompose the problem into sub-domains that can be adequately faced using variable-fidelity models. Reynolds Averaged Navier-Stokes (RANS) solvers adopting actuator discs models to describe turbine rotors are examples of this approach. The perturbation induced by rotor blades is simply imposed or determined by fast solvers like Blade Element Methods (BEM), see *e.g.*, [6]–[8].

An attempt to generalize standard RANS/actuator disc models is the hybrid viscous/inviscid model recently developed at CNR-INM. This is an interactive approach in which an inviscid-flow solver evaluating turbine perturbation is strongly coupled with a Navier-Stokes solver describing the turbulent flow surrounding the turbine. The inviscid flow is solved by a Boundary Integral Equation Method (BIEM). The methodology is valid to study the three-dimensional flow around a turbine in an arbitrary onset flow. Inviscid flow assumptions are overcome by introducing an original Viscous Flow Correction (VFC) model applied to radial distributions of blade loads. The resulting model is referred to as BIEM-VFC.

Compared to full-viscous flow models, the hybrid Navier-Stokes/BIEM-VFC methodology allows to dramatically reduce the computational cost associated to the numerical solution by CFD of the flow region surrounding rotor blades solid walls. The capability of this methodology to describe the interactions among in-line rotors has been discussed in [9]. Although results are promising, it is apparent that the reliability of this approach is largely affected by the capacity of the inviscid-flow model to correctly describe turbine loading and the perturbation induced to the surrounding flow. To this aim, BIEM-VFC validation studies have been done by considering turbine performance measurements from model tests as benchmark data, and results presented in [10], [11].

Aim of the present work is to describe a more comprehensive validation study where CFD is taken as a virtual tank and full viscous flow simulations provide a benchmark dataset. This allows to analyse in details the capability of BIEM-VFC to correctly describe rotor thrust and torque as well as local details of turbine flow over a range of operating conditions. This includes pressure distribution and wall streamlines on the blades surface, and the path of trailing vortices shed in the rotor wake. The CFD model used in the study is a general purpose Navier Stokes solver in-house developed at CNR-INM over more than two decades and extensively validated for a wide range of hydrodynamics problems [12].

In the present analysis, steady flow RANS sim-

Paper ID number: 1840, Conference track: THM. G. Dubbioso (giulioantonino.dubbioso@cnr.it), F. Salvatore (francesco.salvatore@cnr.it), D. Calcagni (danilo.calcagni@cnr.it), Z. Sarichloo (zohreh.sarichloo@insean.cnr.it), R. Muscari (roberto.muscari@cnr.it), are with the Institute for Marine Engineering (former INSEAN) of the Italian National Research Council (CNR), Via di Vallerano, 139, I-00128 Rome, Italy, R. Starzmann (RStarzmann@schottel.de), is with Schottel Hydro GmbH, Mainzer Str. 99, D-56322 Spay, Germany.

ulations describe a single horizontal-axis turbine in uniform onset flow. A three-bladed turbine designed by Schottel Hydro for installation on floating platforms [13] is taken as case study. This turbine has been the subject of extensive experimental work at model scale through tests in flume and towing tanks and at near scale in a tidal site [14]. Results from flume tank tests [15] provide additional benchmark data.

In the following, the BIEM-VFC methodology is described with details of the viscosity correction and trailing vorticity models. The RANS model used to provide benchmark data is also briefly described. Results of the validation study are presented by considering a range of turbine operating conditions from attached blade flow to stall. Limits of applicability of BIEM-VFC and accuracy of results are discussed.

II. The inviscid-flow model by BIEM

The inviscid-flow model proposed here is based on a Boundary Integral Equation Method (BIEM). The methodology is widely used for the hydrodynamic analysis of marine propulsors and the PRO-INS solver developed at CNR-INM has been applied to the analysis of propeller performance and cavitation, see *e.g.*, [17], and [18].

Recently, the methodology has been extended to the hydrodynamic analysis of marine current turbines, and results of validation studies are described in [10], [11]. The extension from propulsion to energy generation devices implies the introduction of dedicated modelling to describe trailing vorticity dynamics and to account for viscosity effects when turbine blades undergo flow separation and stall.

Inviscid-flow modelling assumptions yield that a scalar potential φ can be introduced to represent the perturbation velocity induced by a turbine as an irrotational field $\mathbf{v} = \nabla\varphi$. Navier-Stokes equations are then dramatically simplified to obtain, in incompressible flow conditions, that the mass conservation equation yields the Laplace equation for the velocity potential, while momentum conservation reduces to the Bernoulli equation

$$\frac{\partial\varphi}{\partial t} + \frac{1}{2}\|\nabla\varphi + \mathbf{v}_I\|^2 + \frac{p}{\rho} + gz_0 = \frac{1}{2}\|\mathbf{v}_I\|^2 + \frac{p_0}{\rho}, \quad (1)$$

where p_0 is the free-stream reference pressure and gz_0 is the hydrostatic head. Quantity $\mathbf{v}_I = \mathbf{v}_0 + \Omega\mathbf{e}_x \times \mathbf{x}$ is the inflow velocity at point $\mathbf{x}$ as seen from an observer fixed with blades rotating at angular velocity Ω about an axis parallel to the unit vector $\mathbf{e}_x$. Quantity $\mathbf{v}_0$ denotes the onset flow velocity field, taken as an input. In case of a turbine aligned to an uniform onset flow at speed V, it is $\mathbf{v}_0 = V\mathbf{e}_x$.

The Laplace equation for φ is solved via a boundary integral formulation [19] where problem unknowns are distributed on the body surface and on its *trailing wake*. By potential flow theory for lifting bodies, the trailing wake denotes a zero-thickness layer where vorticity generated by lifting bodies is shed into the downstream flow. Assuming vanishing perturbation at infinite distance, the following boundary integral representation for φ at an arbitrary field point $\mathbf{x}$ is obtained for a turbine with Z blades

$$\begin{aligned} E(\mathbf{x})\,\varphi(\mathbf{x}) &= \int_{\mathcal{S}_T}\left(\frac{\partial\varphi}{\partial n}G - \varphi\frac{\partial G}{\partial n}\right)d\mathcal{S}(\mathbf{y}) \\ &- \int_{\mathcal{S}_W}\Delta\varphi\frac{\partial G}{\partial n}d\mathcal{S}(\mathbf{y}). \end{aligned} \quad (2)$$

where $\mathcal{S}_T$ denotes the turbine solid boundary combining blades surface $\mathcal{S}_B = \sum_i \mathcal{S}_{B_i}(i = 1, ..Z)$ and the nacelle surface $\mathcal{S}_N$, while $\mathcal{S}_W = \sum_i \mathcal{S}_{W_i}$ denotes the trailing wake. Quantity $\mathbf{n}$ is the unit normal to these surfaces, pointing outward on solid boundaries and from pressure to suction sides at blade trailing edges to define the orientation on the wake. The symbol Δ in Eq. (2) is used to denote discontinuity of velocity potential across the trailing wake surface, while $E(\mathbf{x})$ is a function that makes the same equation to be valid for points $\mathbf{x}$ on the body surface ($E = 1/2$) or inside the fluid domain, $E = 1$. Moreover, quantities $G, \partial G/\partial n$ are unit source and dipoles in the unbounded three-dimensional space and depend only from the mutual position between the collocation point $\mathbf{x}$ and the influencing point $\mathbf{y}$ on the boundary surfaces. A distinguishing feature of the present formulation is that analytical expressions from [19] are used to evaluate the exact contributions of source and dipole terms on hyperboloidal quadrilateral surface elements.

Equation (2) is solved with an impermeabilty condition on solid boundaries, $\partial\varphi/\partial n = -\mathbf{v}_I \cdot \mathbf{n}$, and by imposing on the wake surface that vorticity generated on blades is convected downstream. This turns into a condition of the type $\Delta\varphi(\mathbf{x}_W, t) = \Delta\varphi(\mathbf{x}_{TE}(t - \Delta t))$, where Δt is the convection time between a wake point $\mathbf{x}_W$ and the shedding point $\mathbf{x}_{TE}$ at blade trailing edge.

A numerical solution of the Laplace problem for φ is obtained by discretizing surfaces $\mathcal{S}_B$ and $\mathcal{S}_N$ into quadrilateral elements and imposing impermeability conditions for given onset flow. Enforcing discretized Eq. (2) at centroids of solid boundary elements, a linear set of algebraic equations is obtained.

Once the velocity potential is known, the Bernoulli Eq. (1) is used to determine the pressure distribution and the normal stress $(p\,\mathbf{n})$ acting on turbine solid walls (blade and nacelle). Tangential stress $\mathbf{f}_\tau$ is related to viscous friction τ that is missing in the inviscid-flow BIEM solution. Under attached flow conditions, an estimate of τ can be determined through the analogy with a flat plate at zero angle of attack in a fully developed turbulent flow at given Reynolds number [10].

Integrating on blades surface, turbine thrust T and torque Q follow

$$\begin{aligned} T &= \sum_{i=1}^{Z}\int_{R_h}^{R} f'_x dr = \int_{S_B}(-p\mathbf{n} + \mathbf{f}_\tau)\cdot\mathbf{e}_x\, d\mathcal{S}, \\ Q &= \sum_{i=1}^{Z}\int_{R_h}^{R} f'_t\, r\, dr = \int_{S_B}\mathbf{x}\times(-p\mathbf{n} + \mathbf{f}_\tau)\cdot\mathbf{e}_x\, d\mathcal{S} \end{aligned} \quad (3)$$

where R, R_h are, respectively, blade and hub radius. In the expressions above, quantities f'_x and f'_t are introduced to define radial distributions along blade of, respectively, axial and tangential hydrodynamic forces.

Based on the formulation outlined above, further modelling is introduced to determine the trailing wake surface $\mathcal{S}_W$ in Eq. (2), and a correction of blade loads in Eq. (3) taking into account for the effects of boundary layer separation and stall.

A. Trailing wake model

A simple approach typically used in BIEMs is to approximate $\mathcal{S}_W$ with an helicoidal surface whose axial pitch and radial expansion or contraction is defined through semi-empirical or analytical assumptions.

Here, a more physically consistent formulation is proposed in which the actual shape of the wake is determined as a part of the flowfield solution by BIEM. Starting from an initial guess of $\mathcal{S}_W$, the location of nodes of the discretized wake surface is updated by imposing that wake points are shed according to the velocity field resulting from the onset flow and the turbine induced perturbation. The latter is evaluated from a representation of the perturbation velocity $\nabla\varphi$ obtained by taking the gradient of Eq. (2) (with $E = 1$)

$$\begin{aligned}\mathbf{v}_w(\mathbf{x}) &= \int_{\mathcal{S}_T}\left[\frac{\partial\varphi}{\partial n}\nabla_{\mathbf{x}}G - \varphi\nabla_{\mathbf{x}}\left(\frac{\partial G}{\partial n}\right)\right]d\mathcal{S}(\mathbf{y}) \\ &- \int_{\mathcal{S}_W}\Delta\varphi\nabla_{\mathbf{x}}\left(\frac{\partial G}{\partial n}\right)d\mathcal{S}(\mathbf{y}) \qquad (4)\end{aligned}$$

where symbol $\nabla_{\mathbf{x}}$ denotes the gradient operator acting on a wake point $\mathbf{x}$. Once the velocity potential φ on the solid surface $\mathcal{S}_T$ is known from the solution of Eq. (2), quantities in the right-hand side in Eq. (4) are known and the perturbation velocity $\mathbf{v}_w$ at any field point in the wake can be determined. The numerical evaluation of the above expression implies a specific treatment of the gradient of dipole contributions over the wake to avoid contributions tending to infinity as the distance between the influencing point $\mathbf{y}$ and the collocation point $\mathbf{x}$ reduces to zero. A robust formulation is obtained by recasting the dipole gradient on a surface element $\mathcal{S}_{W_n}$ through the Biot-Savart law [17]

$$\nabla_{\mathbf{x}}\int_{\mathcal{S}_{W_n}}\frac{\partial G}{\partial n}\,d\mathcal{S}(\mathbf{y}) = \frac{1}{4\pi}\oint_{\partial\mathcal{S}_{W_n}}\frac{(\mathbf{x}_c-\mathbf{y})\times d\mathbf{y}}{\|\mathbf{x}_c-\mathbf{y}\|^3}, \qquad (5)$$

where $\mathbf{x}_c$ denotes the wake surface element centroid. The velocity distribution resulting from Eqs. (4) and (5) is interpolated at wake grid nodes. Furthermore, the axial position of the tip vortex, corresponding to wake grid nodes shed at blade tip, is updated by imposing shedding at velocity obtained by averaging freestream velocity outside the streamtube, $\mathbf{v}_0 = V\mathbf{e}_x$, and the mean axial velocity evaluated by Eq. (4) inside the streamtube. Such a tip-vortex sheeding model follows the *roll bearing analogy* proposed by Okulov & Sørensen in [20]. The resulting trailing wake model generalizes the formulation introduced in [10], which is used here to determine an initial guess of the wake shape. A trailing wake shape consistent with the perturbed flowfield around the turbine is then obtained by iteratively solving Eqs. (2) and (4) as described.

B. Viscous flow correction to blade loads

The inviscid flow methodology described above fails to describe turbine loads when blade boundary layer undergoes separation and stall. This condition is typical for hydrokinetic turbines when the Tip Speed Ratio (TSR) reduces below the maximum torque point. A simple methodology has been developed in [10] to correct radial distributions of blade loads. To this aim, sectional lift and drag forces evaluated by BIEM under inviscid flow assumptions are compared with forces generated on two-dimensional (2D) profiles representative of blade sections and operating at same angle of attack and Reynolds number of blade sections. The approach is referred to as Viscous Flow Correction (VFC).

By isolating contributions from $\mathcal{S}_W$ in Eq. (4), the velocity $\Delta\mathbf{v}_w$ induced by the trailing vorticity in the wake can be evaluated. Axial and tangential components of $\Delta\mathbf{v}_w$ are used to determine the direction of the actual flow incoming to the blades and the *effective* angle of attack α_e at each blade section, as sketched in Fig. 1, where ϕ denotes the blade pitch

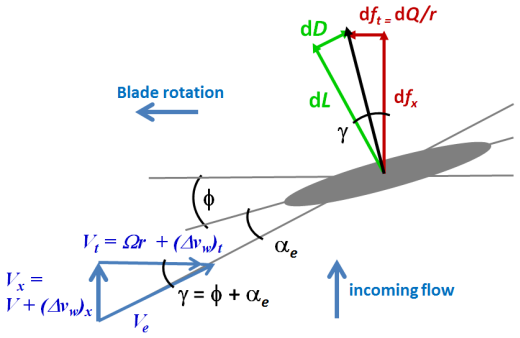

Fig. 1. Inflow velocity components and hydrodynamic force components on turbine blade section at radius r.

The difference between the effective angle of attack and the *nominal* angle of attack where $\mathbf{v}_w$ components are neglected is representative of three-dimensional flow effects at blade sections. Then, an approximated evaluation of lift and drag generated at a given blade section at radius r can be obtained from a 2D model provided that the effective angle of attack α_e is used. In the present model, the X-Foil code by Drela [21] is used to predict lift and drag. This solver, largely used in the analysis of wind and tidal turbines by Blade Element methods (BEM), is based on a BIEM for two-dimensional flows combined with an integral boundary layer solver to predict hydrodynamic loads for attached as well as separated flow including stall.

For a given turbine operating point, flow conditions on blade section at radius r are then determined in terms of radial distributions of the effective angle of attack α_e and of the local Reynolds number

$$Re_r = cV_I/\nu = c\sqrt{(\mathbf{v}_0\cdot\mathbf{e}_x)^2+(\Omega r)^2}/\nu \qquad (6)$$

with c denoting blade chord and ν the kinematic viscosity of water.

Sectional lift $\mathrm{d}L_{2D}$ and drag $\mathrm{d}D_{2D}$ evaluated by X-Foil are compared with corresponding quantities evaluated under inviscid flow conditions, denoted as

$(\ )_{2Dinv}$, and including skin friction contribution by the flat plate analogy as described above. Then, expressions of *correction* factors relating viscous-flow and inviscid-flow sectional loads are obtained as follows

$$\begin{aligned} K_{D}(r) &= \mathrm{d}D_{2D}/\mathrm{d}D_{2Dinv}, \\ K_{L}(r) &= \mathrm{d}L_{2D}/\mathrm{d}L_{2Dinv} \end{aligned} \tag{7}$$

and sectional lift and drag by BIEM are recast as

$$\begin{aligned} \mathrm{d}\hat{L}_p &= \mathcal{K}_{L}\mathrm{d}L_p, & \mathrm{d}\hat{D}_p &= \mathcal{K}_{L}^2\mathrm{d}D_p \\ \mathrm{d}\hat{L}_\tau &= \mathcal{K}_{D}\mathrm{d}L_\tau, & \mathrm{d}\hat{D}_\tau &= \mathcal{K}_{D}\mathrm{d}D_\tau \end{aligned} \tag{8}$$

where symbol $(\hat{})$ labels viscous-flow corrected quantities. In the above expressions, quantities L_p, L_τ denote lift contributions from BIEM obtained by integrating, respectively, normal stress (pressure) and tangential stress (friction). Same meaning holds for drag components D_p, D_τ. Finally, denoting $\gamma = \alpha_e + \phi$ (Fig. 1), viscous flow corrected radial distributions of axial and tangential forces follow (compare with Eq. (3))

$$\begin{aligned} \hat{f}'_x &= \sin\gamma\left(\mathrm{d}\hat{D}_p + \mathrm{d}\hat{D}_\tau\right) + \cos\gamma\left(\mathrm{d}\hat{L}_p + \mathrm{d}\hat{L}_\tau\right) \\ \hat{f}'_t &= -\cos\gamma\left(\mathrm{d}\hat{D}_p + \mathrm{d}\hat{D}_\tau\right) + \sin\gamma\left(\mathrm{d}\hat{L}_p + \mathrm{d}\hat{L}_\tau\right) \end{aligned} \tag{9}$$

A key limitation of the BIEM-VFC model is that viscosity correction applies only to radial distributions of blade loads while no correction is given for local distributions of normal and tangential stress acting over the blades surface. This aspect will be discussed in Section V where results by the present methodology are compared with flowfield predictions by the full viscous-flow solver described in the following section.

III. Virtual towing tank: RANS

Removing the simplifying assumptions of inviscid, irrotational flow, turbine hdrodynamics can be analysed under general mass and momentum conservation equations and the effects of flow viscosity and turbulence on turbine flow and performance are investigated in details. In the present study, the numerical simulation of the flow field is performed by the integration of the Reynolds–Averaged Navier–Stokes equations written in non-dimensional form in the frame of reference fixed to the rotating blades in terms of absolute velocity:

$$\left(\mathbf{u} - \Omega\mathbf{e}_x \times \mathbf{r}\right)\nabla\mathbf{u} + \nabla p - \nabla\cdot\tau = 0$$

where $\mathbf{u}$ is the absolute velocity in the intertial frame of reference, $\mathbf{r} = \mathbf{x} - \mathbf{x}_0$ is the position of point $\mathbf{x}$ with respect to $\mathbf{x}_0$, $\tau = \nu_T\left(\nabla\mathbf{u} + \nabla\mathbf{u}^T\right)$ the stress tensor, $\nu_T = 1/\mathrm{Re} + \nu_t$, ν_t being the turbulent viscosity calculated by the Spalart & Allmaras model [22] and Re the Reynolds number (later defined).

As boundary condition, at solid walls the velocity of the fluid is set equal to the local wall velocity, i.e. $\mathbf{u} = \Omega\mathbf{e}_x \times \mathbf{r}$, at the inflow the velocity is set to the value of the undisturbed flow, $\mathbf{u} = \mathbf{v}_0$, whereas at the outflow the velocity is extrapolated from inner points.

The numerical integration of the governing equations (10) is performed by means of an in–house solver thoroughly described in [23] and in the references therein cited. The methodology is briefly reviewed here for the sake of completeness.

The numerical algorithm is based on a finite volume technique with pressure and velocity co–located at cell centers. The computational domain is partitioned into structured blocks each one subdivided into hexahedrons. Conservation laws are then applied to each hexahedron:

$$\begin{cases} \displaystyle\sum_{i=1}^{6}\int_{\mathcal{S}_i}\mathbf{u}\cdot\mathbf{n}\,dS = 0 \\ \displaystyle\frac{\partial}{\partial t}\int_{\mathcal{V}}\mathbf{u}\,dV + \sum_{i=1}^{6}\int_{\mathcal{S}_i}\left(\mathcal{F}_c - \mathcal{F}_d\right)\cdot\mathbf{n}\,dS = 0 \end{cases} \tag{10}$$

where $\mathcal{S}_i$ is the i-th face of the generic finite volume $\mathcal{V}$ and the fluxes are decomposed into a convective part $\mathcal{F}_c$ and a diffusive term $\mathcal{F}_d$.

A standard second order centered scheme is used for the computation of viscous terms, whereas a centered fourth–order scheme has been applied for the computation of Eulerian terms. Because of the treatment of the viscous terms, the scheme is formally second order accurate in space, although previous numerical experience proved that using a high order approximation of Eulerian terms can remarkably reduce the actual error.

The physical time–derivatives are approximated by a second order accurate, three-point backward finite difference formula. The resulting scheme is fully implicit in time and a dual time stepping approach is adopted for its integration.

The equations are discretized on a block structured grid with partial overlapping. This approach renders domain discretization and grid quality control much easier than with structured meshes with abutting blocks when dealing with complex geometries like the one under investigation. High performance computing is achieved by a hybrid shared (OMP) and distributed (MPI) memory parallelization.

IV. Test case and numerical set-up

The case study selected for the present analysis is a three-bladed fixed-pitch horizontal-axis turbine designed by Schottel Hydro GmbH for installation on floating platforms [13]. This turbine has been the subject of comprehensive experimental studies at model scale (diameter $D = 0.5$ and 1.5 m) and at full scale [14], [15]. Main turbine geometry data are described in [16] and summarized in Table I, while Fig. 2 shows the $D = 0.5$ m model and set-up in the depressurised flume tank at CNR-INM for performance measurements in uniform onset flow ($\mathbf{v}_0 = V\mathbf{e}_x$).

Model test results are used as benchmark in the comparison between numerical predictions by RANS and BIEM-VFC discussed in the following section. Test conditions correspond to onset flow speed $V = 2m/s$ and tip speed ratio $\lambda = \Omega R/V$ from 1 to 10 (with $R = D/2$). Turbine performance is presented as thrust, torque and power coefficients,

$$C_T = \frac{T}{\frac{1}{2}\rho A V^2}, \quad C_Q = \frac{Q}{\frac{1}{2}\rho A V^2 R}, \quad C_P = \frac{\Omega Q}{\frac{1}{2}\rho A V^3} \tag{11}$$

while the pressure distribution over the blade surface is given in terms of the pressure coefficient c_p

$$c_p = (p - p_0) / \frac{1}{2} \rho V_I^2 \tag{12}$$

where $V_I = \sqrt{V^2 + (\Omega r)^2}$ is the nominal inflow speed at radius r along blade span.

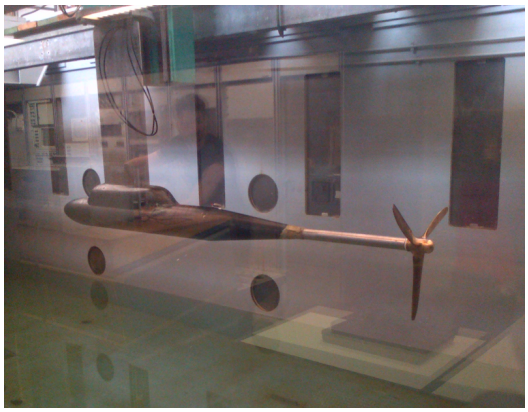

Fig. 2. The Schottel Hydro model turbine during performance tests in the flume tank at CNR-INM.

TABLE I
MODEL TURBINE MAIN GEOMETRY PARAMETERS

Diameter	D	[m]	0.50
Pitch ratio, $r/R = 0.7$	$P_{0.7}/D$	[-]	0.30
Area ratio	A_E/A_0	[-]	0.14
Chord length, $r/R = 0.7$	$c_{0.7}$	[m]	0.04
Rake	ε	[m]	0.00
Skew angle	θ	[deg]	5.45
Number of blades	Z	[-]	3
Hub diameter ratio	d_h/D	[-]	0.10

Both viscous-flow and inviscid-flow simulations describe a single turbine in an unbounded uniform flow. For each flow condition, the Reynolds number is the same as in model tests. The three-dimensional model considered in both RANS and BIEM simulations reproduce the geometry of the $D = 0.5$ m physical model. The only exception is that in the BIEM grid blade root sections have streamlined shape while the actual geometry presents thick sections with blunt trailing edge, see Fig. 3. It should be noted that both RANS and BIEM three-dimensional models present a finite length nacelle, while in the physical model the rotor boss is connected downstream to a dynamometer inside a gondola supported by a stanchion, see Fig. 2.

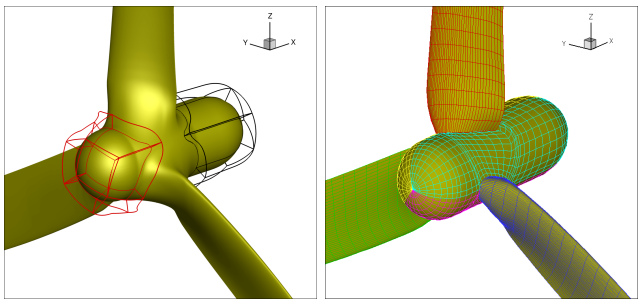

Fig. 3. Detail of blade roots and nacelle in the 3D models used in RANS (left) and BIEM (right) simulations.

C. BIEM: numerical set–up

Blade and nacelle surfaces have been discretized into quadrilateral elements and surface meshes are built using an in-house software. Discretization parameters have been chosen on the basis of a grid sensitivity study on tidal turbines discussed in [10]. Specifically, each blade is discretized into 36 elements chordwise from leading to trailing edges, and 30 elements spanwise, with grid refinement at blades leading edge and tip. The nacelle grid is automatically generated once the blade root is discretized and in the present case this results into 42 and 54 elements, respectively, in circumferential and longitudinal directions. Finally, the wake surface shed by each blade is discretized into 30 elements along radius and 60 elements streamwise per revolution, while 10 revolutions in total are considered. Details of the grid built around the nacelle and in the blade root region are shown in Fig. 3.

Turbine performance in uniform onset flow is studied by steady flow calculations in the frame of reference fixed with rotating blades. Taking advantage of geometry and flow symmetry, discretization parameters above result into a linear problem with 3024 unknowns. The numerical solution for a single tip speed ratio λ with imposed wake geometry takes less than 30 seconds of CPU time on a 2.6 GHz single-core processor. If the wake alignment procedure is used, the CPU time grows proportionally to the number of iterations. For the numerical solutions described in the present work, the iterative procedure converges in 15 to 25 steps with slower convergence at high tip speed ratio where trailing wake effects are stronger, as it will be discussed later.

D. RANS: numerical set–up

Akin BIEM, RANS simulations are performed in a frame of reference fixed with rotating blades, but in this case a time-marching solution is calculated. The time step is chosen to have a rotation of two degrees for the propeller ($dt = 0.014373$) per integration step. All quantities are cast in non–dimensional form.

Figure 4 shows the building blocks of the mesh. For each blade and for both the fore and the aft parts of the hub, “O-grid” topology is chosen. In particular, the blade is discretized by two overlapping ”O-grid” used for the main body (from the blade root to r/R=0.95) and the tip. The near field of the wake is discretized with two adjacent cartesian blocks. The block covering the turbine has a finer grid in order to achieve the best overlap with grid blocks around the blades. The remaining part of the mesh is made by concentric toroidal blocks covering the whole domain.

The boundary layer is fully resolved, the first point being set at a distance from the wall such that $y^+ < 1$ in wall unit. The whole grid has 41M cells in total and the relative weight of grid blocks is detailed in table II. Results discussed in the present paper refer to the medium grid level, while computations on the finest mesh are in progress. Computations are carried out on a parallel machine (processors Intel Xeon 3GHz) by hybrid 4 MPI and 2 OMP processes. About 60 hours

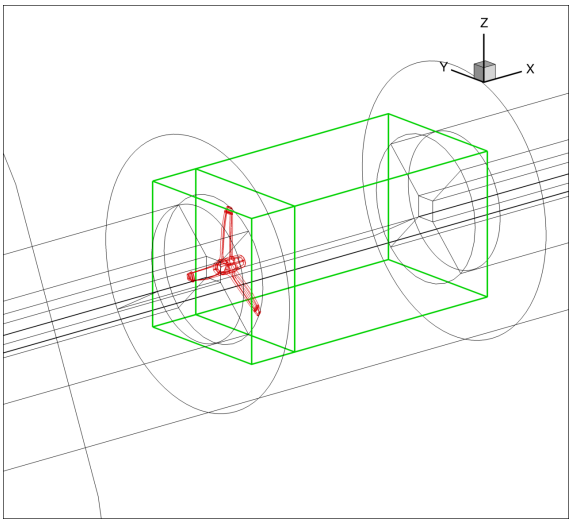

(a) Overview of RANS grid blocking layout

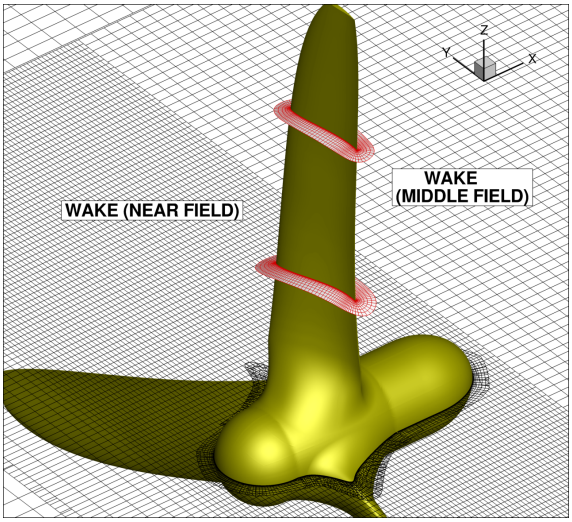

(b) Close-up in the near field

Fig. 4. RANS grid topology

TABLE II
DISTRIBUTION OF COMPUTATIONAL CELLS

GRID ELEMENTS		
rotor blades	8M	(19.5%)
rotor hub	1M	(2.0%)
near field (propeller)	18M	(43%)
medium field (wake)	11M	(27%)
far field (background)	3M	(6%)
total	41.00M	

corresponding to 15 turbine revolutions are required to achieve a complete stabilization of loads and wakefield.

V. Numerical Results

Turbine performance in uniform onset flow is studied by BIEM and BIEM-VFC and results are analysed by comparing with full viscous flow simulations by RANS and, limiting to global performance, with experimental data. Measurements from flume tank tests [15] provide mean values as well as standard deviation of thrust and torque over a Tip Speed Ratio (λ or TSR) range from 0 to 10. BIEM and BIEM-VFC results span from TSR 1 to 10 with 0.5 step, while RANS calculations are limited to TSR values 2, 3, 4, 5, 6, 8.

Turbine loads predicted by BIEM under inviscid-flow assumptions are corrected to account for viscosity effects as decribed in Section II-B. Main results of the VFC procedure applied to the present case study are briefly outlined here. The inviscid-flow solution is used to estimate radial distributions of the effective angle of attack α_e and of the Reynolds number Re_r at blade sections. Considering the variability of these quantities over the TSR range of interest, contour maps shown in Fig. 5 are obtained.

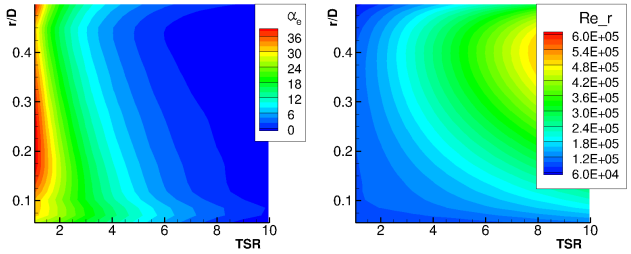

Fig. 5. Radial distribution of effective angle of attack α_e (left) and of Reynolds number Re_r (right) evaluated by BIEM as a function of radius r and of tip speed ratio (TSR).

A two-dimensional (2D) profile corresponding to the turbine blade section at 70% of radius is taken as representative of the hydrodynamic characteristics of all sections. Profile polar curves are determined over effective angle of attack and Reynolds number ranges in Fig. 5. Results are shown in Fig. 6, where for angle of attack below 15 degrees, lift and drag are predicted by X-Foil, while at higher incidence the extrapolation procedure described in [11] is applied. Using Eqs. (7), correction factors K_L, K_D are determined at each blade section, and radial loads by inviscid-flow BIEM are corrected using Eqs. (8) and (9). Distributions of correction factors K_L, K_D at relevant angle of attack and Reynolds number are shown in Fig. 7.

Turbine thrust, torque and power coefficients calculated by inviscid-flow BIEM and by BIEM-VFC are plotted in Fig. 8 and compared with results by RANS and by model tests.

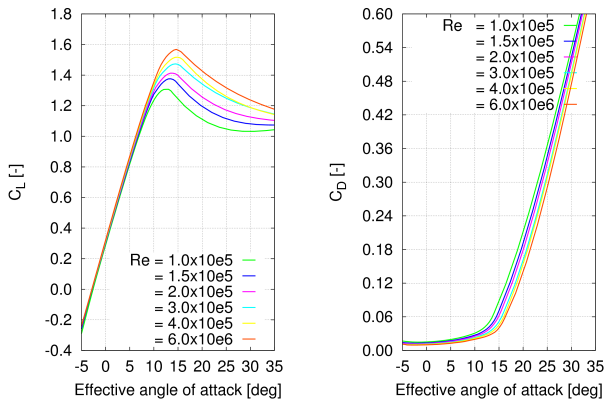

Fig. 6. Lift (left) and drag (right) curves of turbine blade section at 70% of span. X-Foil predictions between -5 and 15 degrees and extrapolated data between 15 and 35 degrees.

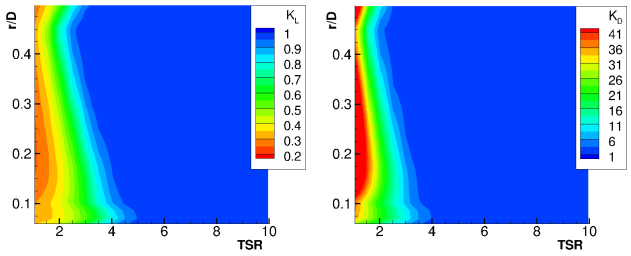

Fig. 7. Correction factors for radial contributions to lift (K_L, left) and drag (K_D, right) as a function of radius r and of TSR .

Torque coefficient C_Q (top Fig. 8) is analysed first, in that its variability with respect to TSR allows to clearly identify two regions with distinct phenomenologies affecting turbine performance. Results of model tests show that torque increases as TSR reduces from 10 to 3.5, while further reductions of TSR correspond to an abrupt torque loss. This trend reveals that blade flow is mostly attached for TSR higher than 3.5-4, while viscosity-induced separation and stall effects become more and more important as TSR reduces from 3.5 to zero. As expected, inviscid-flow results by BIEM completely miss the effects of flow separation and stall and predicted torque presents an unphysical trend at TSR below 3.5. In contrast to this, transition from attached flow to stall is fairly captured by the BIEM-VFC model. In particular, comparing inviscid-flow results with those including the viscous-flow correction, it may be noted that viscosity effects on torque become non negligible at TSR lower than 5, and BIEM-VFC predicts a significant torque drop between TSR 2.5 and 3. Full viscous flow solutions by RANS are in good agreement with measurements except for case TSR = 3, where predicted torque is significantly higher than the experimental value and very close to inviscid-flow BIEM results. This can be explained by a delayed prediction of massive separation and stall on blades as flow conditions vary from high to low TSR. At TSR = 4 and higher, BIEM-VFC results are in good agreement with both model tests and RANS, while torque is overestimated at very high TSR.

The sudden transition from attached blade flow to stall when TSR reduces from 4 to 3 is less apparent in power and thrust curves, bottom Fig. 8. For these quantities, RANS reproduces experimental data with good accuracy. The only exception is power at TSR between 3 and 4 where stall delay described above determines overestimated predictions of measured power, while the effect on thrust is negligible. The inclusion of viscous flow correction on BIEM determines very good predictions of thrust and torque between TSR 3 and 7.5. The same correction at lower TSR provides satisfactory results for power, while viscosity correction on thrust is overestimated.

As already observed for torque (and hence for power), thrust is overestimated at very high TSR. In order to explain these discrepancies, global performance data from model tests are not helpful, while the comparison of flow quantities predicted by BIEM-VFC and by RANS makes possible an in-depth analysis. Three representative operating conditions are identified for this analysis: attached flow at maximum power point (TSR = 5) and at high speed (TSR = 8), and turbine stall at TSR = 2.

E. Attached flow: TSR = 5 and 8

Results of turbine performance discussed above highlight that for TSR = 5 and higher, blade flow is mostly attached and the viscous-flow correction to blade loads is small. Under attached flow conditions, the pressure on a lifting surface is not affected by viscosity and the Bernoulli Equation (1) is valid. Hence, blade pressure distributions predicted by inviscid-flow BIEM can be compared with the RANS solution.

As described in Section II-B, it is important to stress here that the viscous-flow correction applies only to radial distributions of loads integrated at blade sections and hence pressure distributions by BIEM and by BIEM-VFC are equivalent regardless of the TSR considered. Figure 9, present contour maps of the pressure coefficient c_p defined in Eq. (12) evaluated by BIEM and by RANS for the two cases TSR = 5 and 8. A very good agreement between the two solutions is apparent for both TSR cases on blade suction and pressure sides. Significant discrepancies are localised only at blade root, where solid wall geometry considered in RANS and BIEM grids differ, as shown in Fig. 3.

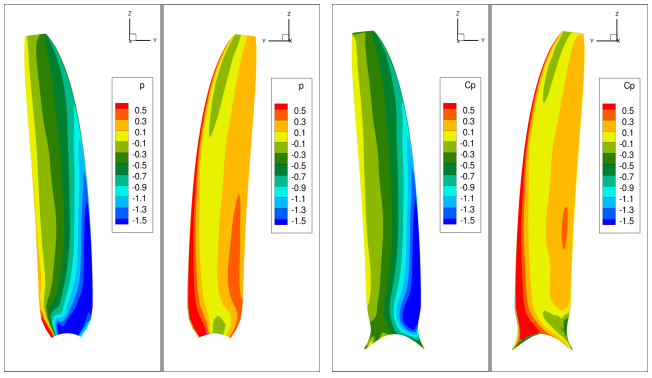

(a) BIEM, TSR=5 (b) RANS, TSR=5

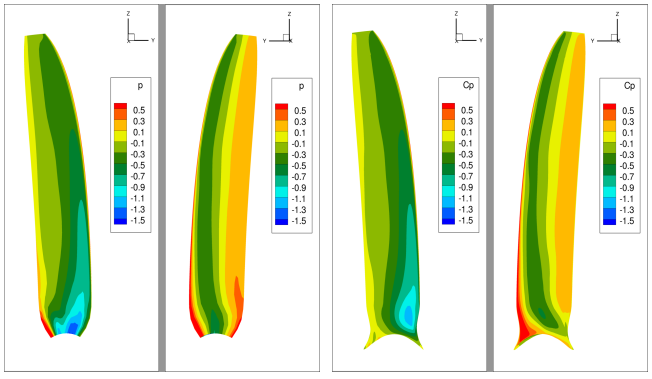

(c) BIEM, TSR=8 (d) RANS, TSR=8

Fig. 9. Pressure coefficient c_p distribution on blade suction side (left) and pressure side (right): BIEM and RANS solutions compared.

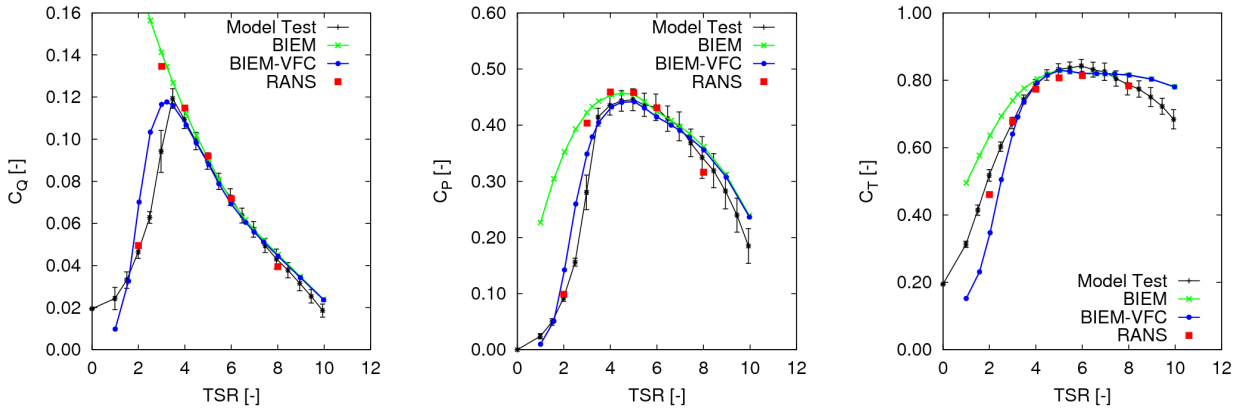

Fig. 8. Turbine performance curves predicted by BIEM, BIEM-VFC compared with RANS and model test results from [15]. From left to right: torque, power, thrust coefficients.

A quantitative comparison of pressure distributions on blade sections at radius $r/R = 0.7, 0.9$ is shown in Fig. 10. Plots confirm that discrepancies between distributions by BIEM and by RANS solutions are very small. In particular, negative pressure peaks at blade leading edge by the two models are fully comparable, while differences are localised in the trailing edge region, where BIEM overestimates the pressure gap between suction and pressure sides. This determines local higher blade loading contributions that are expected to have a larger effect at high TSR, where blades tend to be unloaded. This may explain overestimated thrust and torque at high TSR observed in Fig. 8. The analysis of the BIEM solution highlights that pressure distributions at blade trailing edge can be significantly improved by local refinement of the grid used in present calculations.

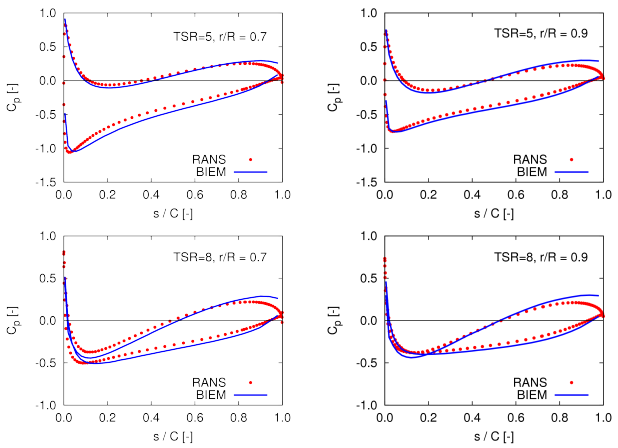

Fig. 10. Pressure coefficient c_p distribution at blade section $r/R = 0.7$ (left) and $r/R = 0.9$ (right) at TSR = 5 (top) and TSR = 8 (bottom). BIEM and RANS solutions compared.

The presence of attached flow throughout the blade surface in the two operating conditions at TSR = 5, 8 is confirmed by flow streamlines at solid wall. The TSR = 5 case is illustrated in Fig. 11 as representative of attached flow conditions. In both RANS and BIEM solutions, streamlines run at almost constant radius over all blade span. As expected, cross flow components are present at blade tip where flows from blade pressure and suction sides merge and form the tip vortex. Significant cross flow is also noted in the RANS solution at blade root, while this is almost negligible from BIEM. As already mentioned, a quantitative comparison of flow quantities at blade root is impossible due to differences in the geometry used in BIEM and RANS grids.

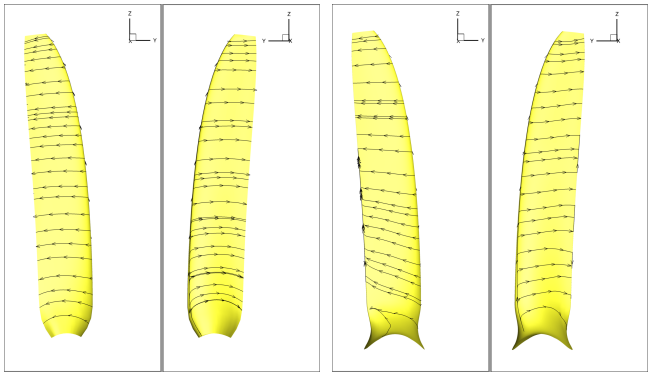

(a) BIEM (b) RANS

Fig. 11. Streamlines at solid wall on blade suction side (left) and pressure side (right) at TSR = 5: BIEM and RANS solutions compared.

Although blade flow shows small cross flow components, three-dimensional effects exist and are related to the velocity perturbation induced by the trailing vorticity path shed at blade trailing edge and tip. The impact of trailing vorticity on blade flow can be analysed by comparing radial distributions of nominal and effective angles of attack, respectively, α_0 and α_e as defined in Section II. Figure 12 compares α_0 and α_e distributions along blade span for cases TSR = 5 and 8. The velocity perturbation induced by trailing vorticity determines a reduction of the angle of attack that varies from few degrees at blade tip to 5-10 degrees at root and for a given radial position along the span grows with blade loading.

Results above show that under attached boundary layer conditions, cross flow velocity components are generally small. Then, the flow at a blade section at given radius r can be approximated by a 2D flow about

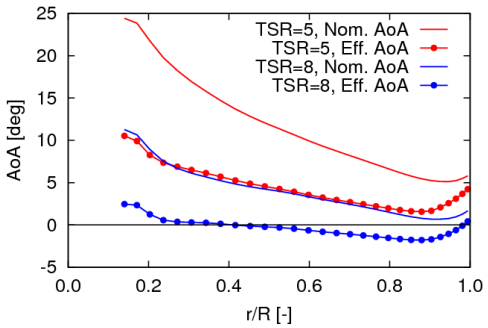

Fig. 12. Nominal and effective angle of attack (AoA) distributions along blade span at TSR = 5 and 8.

the same section at angle of attack equal to the effective angle of attack at radius r from the BIEM solution. The correspondence between 3D blade flow and 2D flow at *equivalent* angle of attack can be analysed by comparing pressure distributions by BIEM with those obtained by the 2D X-Foil solver. Representative results for blade section at $r/R = 0.7$ and TSR = 3, 4, 5, 8 are shown in Fig. 13. As expected, BIEM and X-Foil predictions are very similar, except for the leading edge region where laminar flow is found by the X-Foil solution. Blade pressure predictions by RANS are also plotted for comparison. Recalling performance curves in Fig 8, these TSR values correspond to globally attached flow conditions in RANS simulations and there is a general agreement of C_p by RANS with both BIEM and X-Foil. Differences observed at TSR = 3 (top left Fig. 13) reveal that some flow separation effects on blade suction side are captured by the 3D RANS solution that are neglected by the 2D X-Foil solution. Apart from these small differences, the comparison demonstrates that under attached or weakly separated flow conditions, blade pressure distributions can be reasonably approximated by 2D flow solutions provided that the effective angle of attack accounting for 3D flow effects is used. When massive flow separation and stall occurs, such a correspondence between 2D and 3D flow disappears as described in the following subsection.

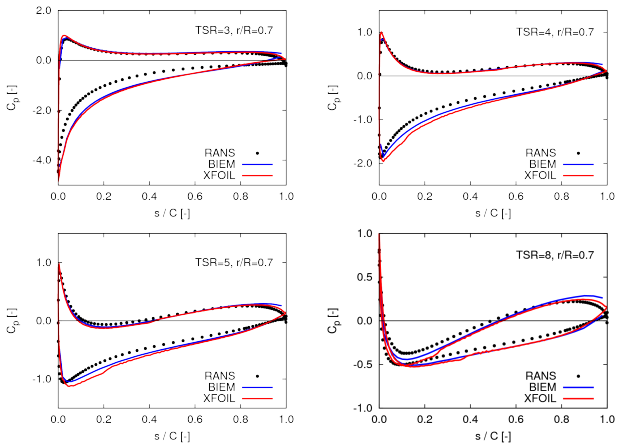

Fig. 13. Pressure coefficient c_p distribution at blade section $r/R = 0.7$ and TSR values 3, 4, 5, 8. Turbine flow solutions by BIEM and RANS compared with 2D flow simulations by X-Foil.

To complete the analysis of BIEM and BIEM-VFC in conditions where the blade surface is free from massive flow separation, results of the trailing wake model described in Section II-A are briefly discussed. Regarding this aspect, it is worth noting that the present inviscid flow model strongly depends from the definition of the wake surface $\mathcal{S}_W$ being used in the numerical solution of Eqs. (2) and (4). The accuracy of trailing wake modelling is then fundamental for the BIEM solution *per se* and to correctly determine the effective angle of attack that is used in the viscous flow correction model as described in II-B. The impact of trailing wake modelling on the BIEM or BIEM-VFC solution is particularly strong at high TSR, where the out-of-plane component of the wake shedding velocity is proportionally small and wake vortices in the near wake stand very close to the rotor blades. Numerical studies not reported here have demonstrated that using a prescribed wake model with inaccurate definition of axial and radial position of shed vorticity may turn into wrong predictions of turbine power of 20-30% and more at medium/high TSR.

The comparison of the trailing wake surface predicted by BIEM with the wake field obtained from RANS simulations allows to analyse the capability of BIEM to provide a physically consistent description of the vorticity path shed downstream of the turbine. To this purpose, Fig. 14 presents the out-of-plane vorticity field evaluated by RANS on a longitudinal plane through the turbine axis and the wake surface $\mathcal{S}_W$ evaluated by the BIEM trailing wake model. For the sake of clarity only the $\mathcal{S}_W$ portion shed by one blade and truncated after four revolutions is plotted. Flow conditions at TSR 5 and 8 are considered. At first glance, the impact of TSR on the wake shedding velocity mentioned above is apparent. At TSR = 5, the first two revolutions of the BIEM wake surface are consistent with the location of the tip vortex resulting from the RANS solution. In particular, the radial expansion of the wake is correctly described, while the axial shedding is slightly slower than in the RANS solution. Downstream of two wake revolutions, vorticity in the tip vortex region is diffused in the RANS solution and only the agreement between radial expansion of the streamtube predicted by BIEM and RANS can be assessed. At higher TSR, bottom Fig. 14, blade loading reduces and hence trailing vorticity is weaker. From the RANS solution only the first wake revolution can be clearly distinguished from the vorticity field and in this region the trailing wake model by BIEM correctly predicts both axial shedding and radial expansion.

F. Stalled flow: TSR = 2

The analysis of results by BIEM with respect to RANS is now extended to the case of blade flow characterized by strong vicosity effects. Results of turbine performance in Fig.8 reveal that at TSR = 2 turbine blades undergo massive flow separation and stall. In such conditions, the viscous flow correction (VFC) model described in Section II-B provides an estimate of flow separation and stall effects on the radial distribution

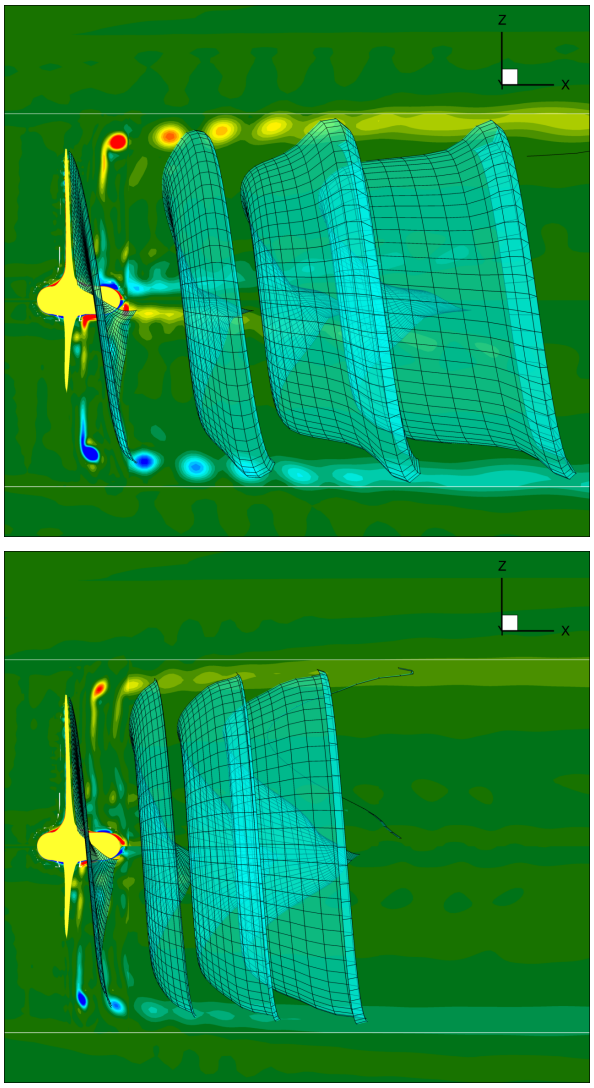

Fig. 14. Turbine wake flow. Axial vorticity distribution over a longitudinal plane by RANS and trailing wake surface shed by one blade from the BIEM solution. TSR = 5 (top) and TSR = 8 (bottom).

of blade loads evaluated by the inviscid-flow BIEM. As already mentioned, in the present version of the model, the viscous flow correction has no effect on velocity and pressure distributions by BIEM and hence comparisons with RANS at TSR = 2 are presented here only to identify the range of validity of the methodology.

Passing from attached flow to stall, the topology of the flow on the blade surface changes dramatically, with occurrence of strong flow components directed spanwise along the blade. This phenomenology typical of finite-span lifting surfaces undergoing massive separation and stall is clearly illustrated by solid wall streamlines in right Fig. 15 where RANS results are plotted. In particular, separated flow spans from root to tip on the blade suction side, while the flow remains attached on the pressure side. As expected, in this case the BIEM solution is very similar to those obtained at higher TSR under attached flow conditions (Fig. 11) and streamlines are directed chordwise throughout the blade surface. In the BIEM solution, cross flow distortion is limited to the tip where, neglecting viscosity effects, an unphysical strong tip vortex is formed.

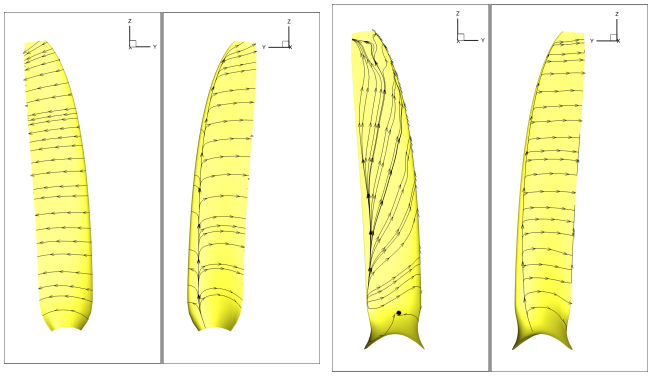

(a) BIEM (b) RANS

Fig. 15. Streamlines at solid wall on blade suction (left) and pressure side (right) at TSR = 2: BIEM and RANS solutions compared.

The effects of massive separation on the blade surface determines very different pressure distributions from RANS and BIEM predictions, as shown in Fig. 16. As already apparent from streamlines, flow separation occurs only on blade suction side, while the boundary layer is mostly attached on the suction side. It is interesting to observe that also in the stalled turbine condition, C_p predictions by BIEM are comparable with those by RANS in blade surface regions where the flow is attached. This is confirmed by pressure distributions at blade sections $r/R = 0.7$ and 0.9 in Fig. 17. From these plots it may be noted that flow separation at leading edge suction side prevents the formation of a strong negative pressure peak that is present in inviscid-flow calculations by BIEM. On the pressure side, BIEM and RANS solutions are very similar.

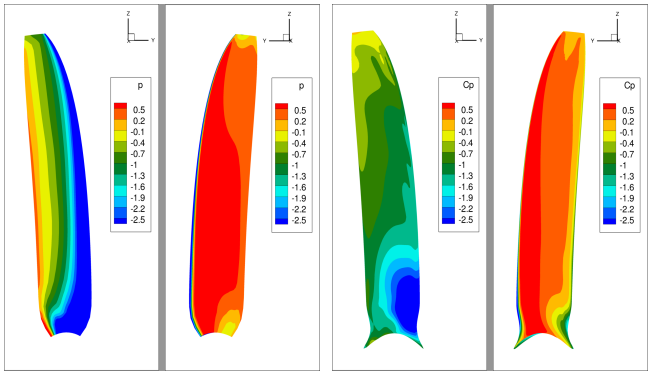

(a) BIEM (b) RANS

Fig. 16. Pressure coefficient c_p distribution on blade suction side (left) and pressure side (right) at TSR=2: BIEM and RANS solutions compared.

VI. Concluding Remarks

The assessment of a tidal turbine hydrodynamics model based on a Boundary Integral Equation formulation with viscous flow correction (BIEM-VFC) has been addressed. In particular, a validation study based on experimental data combined with results of CFD simulations has been performed. While model tests

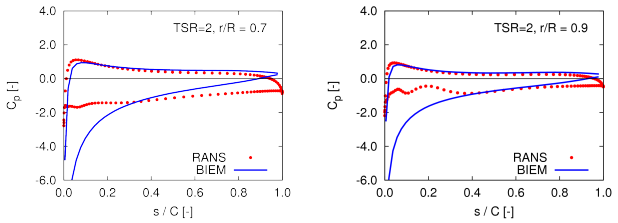

Fig. 17. Pressure coefficient c_p distribution at blade section $r/R = 0.7$ (left) and $r/R = 0.9$ (right). BIEM and RANS solutions at TSR = 2 compared.

provide information on global turbine performance, the numerical solution by CFD allows to perform an in-depth analysis where local flow quantities by BIEM-VFC can be compared and the physical consistency of the solution investigated.

An in-house developed RANS solver has been used in the study and a three-bladed horizontal axis tidal turbine designed by Schottel Hydro has been considered as test case. Numerical results by BIEM-VFC have been analysed in terms of turbine thrust, torque and power over a full range of operating conditions in uniform onset flow. In addition to this, pressure distributions and flow streamlines over the blade surfaces have been analysed by comparing results by BIEM-VFC with RANS simulations. Similarly, trailing wake modelling by BIEM-VFC has been analysed with respect to shed vorticity predictions by RANS.

Main findings can be summarised as follows:

- BIEM-VFC provides reliable predictions of turbine thrust and power over a range of operating conditions where viscosity effects are significant but blades are free from massive separation and stall;
- in this condition, pressure distribution and streamlines on the blade surface by BIEM-VFC are fully validated against results by RANS;
- similarly, trailing wake modelling allows to correctly describe both axial shedding and radial expansion of shed vorticity;
- when the turbine blades are in stall, the viscous flow correction model correctly describes the effects of massive flow separation on power, while a trend to overestimate thrust loss at very low tip speed ratio (TSR) is observed;
- in this condition, pressure distribution and streamlines by BIEM-VFC completely miss separated flow effects but agreement with RANS is still good considering blade surface regions where the flow remains attached or weakly separated.

For the present case study, the peak power condition occurs at TSR between 4 and 6, and stall-induced performance loss occurs at TSR 3 and lower. Results of the validation study highlight that BIEM-VFC predictions of both global and local flow quantities are comparable with those from a full viscous flow solution for TSR higher than 3. In this range of operating conditions, BIEM-VFC can be used to determine local flow information that are typically missing in fast turbine hydrodynamics solvers based on Blade Element Methods. As example, blade pressure distributions can be used to investigate turbine cavitation inception as well as to provide hydrodynamic loading distributions necessary for fluid-structure interaction studies. For TSR conditions corresponding to blade stall, BIEM-VFC provides realistic estimates of global turbine loads, while no information can be derived for local flow quantitities.

Further BIEM-VFC model assessment studies based on comparisons with CFD results will be performed to achieve a comprehensive understanding of the range of applicability of the methodology as an accurate and computational efficient turbine analysis and design tool. Work is also underway to generalize the viscosity correction model in order to have a strong coupling with the iterative trailing wake alignment procedure presented in this study.

ACKNOWLEDGEMENT

The computational study has been carried out in the framework of CNR Project ULYSSES (Underpin LaboratorY for Studies on Sea Energy Systems). Model tests have been funded by Invest North Ireland (INI) under the TTT3 Project.

REFERENCES

[1] T. Blackmore, L. Myers, and A. Bahaj, "Effects of turbulence on tidal turbines: Implications to performance, blade loads, and condition monitoring," *Int. Journal of Marine Energy*, vol. 14, pp. 1–26, 2016.

[2] P. Mycek, G. Gaurier, G. Germain, G. Pinon, and E. Rivolaen, "Experimental study of the turbulence intensity effects on marine current turbines behaviour. part ii: two interacting turbines," *Renewable Energy*, vol. 68, pp. 876–892, 2014.

[3] W. Koh and E. Ng, "A cfd study on the performance of a tidal turbine under various flow and blockage conditions," *Renewable Energy*, vol. 107, pp. 124–137, 2017.

[4] U. Ahmed, D. Apsley, I. Afgan, T. Stallard, and P. Stansby, "Fluctuating loads on a tidal turbine due to velocity shear and turbulence: Comparison of cfd with field data," *Renewable Energy*, vol. 112, pp. 235–246, 2017.

[5] N. Martin and T. Longbin, "Three dimensional tidal turbine array simulations using openfoam with dynamic mesh," *Ocean Engineering*, vol. 147, pp. 629–646, 2018.

[6] M. Edmunds, R. Malki, A. J. Williams, I. Masters, and T. N. Croft, "Aspects of tidal stream turbine modelling in the natural environment using a coupled bem-cfd model," *Journal of Marine Energy*, vol. 7, pp. 20–42, 2014.

[7] M. Shives and C. Crawford, "Tuned actuator disk approach for predicting tidal turbine performance with wake interaction," *Journal of Marine Energy*, vol. 17, pp. 1–20, 2017.

[8] D. Apsley, T. Stallard, and P. Stansby, "Actuator line cfd modeling of tidal-stream turbines in arrays with experimental evaluation," *Int.J.of Ocean Engineering and Marine Energy,*, pp. 1–13, 2018.

[9] F. Salvatore, D. Calcagni, and Z. Sarichloo, "Development of a viscous/inviscid hydrodynamics model for single turbines and arrays," in *Proc. EWTEC'17, Twelfth European wave and Tidal Energy Conference*, Cork, Ireland, 2017.

[10] F. Salvatore, Z. Sarichloo, and D. Calcagni, "Marine turbine hydrodynamics by a boundary element method with viscous flow correction." *J. Marine Science and Enginering*, vol. 6(2), 2018.

[11] Z. Sarichloo, F. Salvatore, F. Di Felice, M. Costanzo, R. Starzmann, and C. Frost, "Computational analysis and experimental verification of a boundary integral equation model for tidal turbines," in *Proc. of RENEW'18, Third Int. Conference on Renewable Energy Offshore*, Lisbon, Portugal, 2018.

[12] R. Muscari, G. Dubbioso, and A. Di Mascio, "Analysis of the flow field around a rudder in the wake of a simplified marine propeller," *Journal of Fluid Mechanics*, vol. 814, pp. 547–569, 2017.

[13] P. Jeffcoate and J. McDowell, "Performance of plat-i, a floating tidal energy platform for inshore applications," in *Proc. EWTEC'17, Twelfth European wave and Tidal Energy Conference*, Cork, Ireland, 2017.

[14] C. Frost, I. Benson, B. Elsäßer, R. Starzmann, and T. Whittaker, "Mitigating uncertainty in tidal turbine performance characteristics from experimental testing," in *Proc. EWTEC'17, Twelfth European wave and Tidal Energy Conference*, Cork, Ireland, 2017.
[15] F. Di Felice, M. Costanzo, M. Fortunati, Z. Sarichloo, and F. Salvatore, "Hydrodynamic performance measurements of Schottel Hydro model turbine," CNR-INSEAN, Rome, Italy, Tech. Rep. 2017-PR-002, 2017.
[16] N. Kaufmann, T. Carolus, and R. Starzmann, "An enhanced and validated performance and cavitation prediction model for horizontal axis tidal turbines," *J. International Journal of Marine Energy*, vol. 19, pp. 145–163, 2017.
[17] F. Salvatore, Greco, L., and D. Calcagni, "Computational analysis of marine propeller performance and cavitation by using an inviscid-flow bem model," in *Proc. 2nd International Symposium on Marine Propulsion SMP'11*, Hamburg, Germany, 2011.
[18] F. Pereira, F. Salvatore, and F. Di Felice, "Measurement and modelling of propeller cavitation in uniform inflow." *Fluids Eng.*, vol. 126(4), pp. 671–679, 2004.
[19] L. Morino, "Boundary integral equations in aerodynamics." *J. Appl. Mech. Rev.*, vol. 46(8), pp. 445–466, 1993.
[20] V. Okulov and J. Sørensen, "Maximum efficiency of wind turbine rotors using joukowsky and betz approaches." *J. Fluid Mech.*, vol. 649, pp. 497–508, 2010.
[21] M. Drela, "Xfoil: An analysis and design system for low reynolds number airfoils. in *Low Reynolds Number Aerodynamics*." *Lecture Notes in Engineering*, vol. 54, pp. 1–12, 1989.
[22] P. R. Spalart, S. R. Allmaras, "A One-Equation Turbulence Model for Aerodynamic Flows," *La Recherche Aérospatiale*, vol. 1, pp. 5–21, 1994.
[23] R. Muscari, A. Di Mascio, and R. Verzicco, "Modeling of vortex dynamics in the wake of a marine propeller," *Computational Fluids*, vol. 73, pp. 65–79, 2013.